

# Properties and dynamics of Jupiter's gossamer rings from Galileo, Voyager, Hubble and Keck images

Mark R. Showalter<sup>a,\*</sup>, Imke de Pater<sup>b</sup>, Giuli Verbanac<sup>c</sup>, Douglas P. Hamilton<sup>d</sup>, Joseph A. Burns<sup>e</sup>

<sup>a</sup> SETI Institute, 515 North Whisman Road, Mountain View, CA 94043, USA

<sup>b</sup> University of California, 601 Campbell Hall, Berkeley, CA 94720, USA

<sup>c</sup> Faculty of Science, Geophysical Institute "Andrija Mohorovicic," Horvatovac bb 10000, Zagreb, Croatia

<sup>d</sup> Department of Astronomy, University of Maryland, College Park, MD 20742, USA

<sup>e</sup> Department of Astronomy, Cornell University, 418 Space Sciences Building, Ithaca, NY 14853, USA

Received 30 December 2005; revised 28 August 2007

Available online 10 January 2008

## Abstract

We present a comprehensive examination of Jupiter's "gossamer" rings based on images from Voyager, Galileo, the Hubble Space Telescope and the W.M. Keck Telescope. We compare our results to the simple dynamical model of Burns et al. [Burns, J.A., Showalter, M.R., Hamilton, D.P., Nicholson, P.D., de Pater, I., Ockert-Bell, M., Thomas, P., 1999. *Science* 284, 1146–1150] in which dust is ejected from Amalthea and Thebe and then evolves inward under Poynting–Robertson drag. The ring follows many predictions of the model rather well, including a linear reduction in thickness with decreasing radius. However, some deviations from the model are noted. For example, additional material appears to be concentrated just interior to the orbits of the two moons. At least in the case of Amalthea's ring, that material is in the same orbital plane as Amalthea's inclined orbit and may be trapped at the Lagrange points. Thebe's ring shows much larger vertical excursions from the model, which may be related to perturbations by several strong Lorentz resonances. Photometry is consistent with the dust obeying a relatively flat power-law size distribution, very similar to dust in the main ring. However, the very low backscatter reflectivity of the ring, and the flat phase curve of the ring at low phase angles, require that the ring be composed of distinctly non-spherical particles.

© 2007 Elsevier Inc. All rights reserved.

**Keywords:** Planetary rings; Jupiter, rings; Hubble Space Telescope observations; Planetary dynamics; Photometry

## 1. Introduction

Jupiter's "gossamer" rings were discovered by Showalter et al. (1985) in a single Voyager image. They were seen extending outward from the main jovian ring but only a few percent as bright. The name was originally chosen because "gossamer" seemed the only suitable adjective to describe a ring far fainter than the (already exceedingly faint) main ring of Jupiter; Burns et al. (1984) had already applied other colorful adjectives, including "ethereal" and "diaphanous," to the main ring. This name has gone on to become its quasi-official moniker.

This ring is composed almost exclusively of micron-sized dust, based on the fact that the ring was only detectable by Voyager at high phase angles, where fine dust grains diffract most of their light. The high dust content is a trait this ring shares with Jupiter's main ring and halo (Showalter et al., 1987).

Showalter et al. (1985) interpreted the system as a single thin, flat ring extending outward to slightly beyond the orbit of Thebe. Its detailed structure was revealed more clearly in edge-on images from Galileo in October 1997 (Ockert-Bell et al., 1999). The system actually consists of two overlapping rings, one bounded by Amalthea and the other by Thebe. Burns et al. (1999) showed in detail how the rings could be generated as dust ejected by each of these moons, which then evolves inward under Poynting–Robertson (henceforth PR) drag while preserving its initial inclination. The rings' most prominent features,

\* Corresponding author. Fax: +1 650 962 9419.

E-mail addresses: [mshowalter@seti.org](mailto:mshowalter@seti.org) (M.R. Showalter), [imke@astron.berkeley.edu](mailto:imke@astron.berkeley.edu) (I. de Pater), [verbanac@irb.hr](mailto:verbanac@irb.hr) (G. Verbanac), [hamilton@astro.umd.edu](mailto:hamilton@astro.umd.edu) (D.P. Hamilton), [jab16@cornell.edu](mailto:jab16@cornell.edu) (J.A. Burns).



Fig. 1. A mosaic of the two gossamer ring images from Galileo's C3 encounter, taken on November 9, 1996. Images C03689915.00 (left) and C03689915.22 (right) show the over-exposed outer tip of the main ring, with the Amalthea ring extending outward to the right. The phase angle is  $179.2^\circ$  and the ring opening angle is  $0.5^\circ$ .

including their vertical and radial profiles, are all consistent with this model.

However, the images provide some suspicions that the reality may not be quite as simple as the Burns et al. (1999) model. First, the Thebe ring shows a very faint outward extension, contradicting the prediction that dust from Thebe should evolve exclusively inward. Second, the Amalthea ring shows a marked vertical asymmetry. Also, limited data obtained by the Dust Detector during Galileo's November 2002 passage through the gossamer rings suggest an inner dropoff to Thebe's dust population (Krüger, 2003; Krüger et al., 2003, 2005). Numerical integrations also raise questions—Burns et al. (2004) and Hamilton et al. (1998) find that micron-sized grains, when electrically charged by solar photons and the local plasma, ought to be scattered by the numerous Lorentz resonances distributed throughout the region.

In this paper, we explore these properties of the gossamer rings in greater detail, via a more complete analysis of the best available data from the Galileo, Voyager 2, the Hubble Space Telescope (HST) and the W.M. Keck Telescope on Mauna Kea. The primary goal is to ascertain how well the current model conforms to the data, using deviations to illuminate the nature of any additional physical processes that may be at work. We also employ the limited available photometry to place, for the first time, quantitative constraints on the particle sizes in the gossamer rings.

## 2. Image summary

### 2.1. Galileo images

The Galileo spacecraft imaged the gossamer rings only twice during its tour of the jovian system. During the C3 and C10 encounters it passed through Jupiter's shadow, making it safe to point the camera close enough to the Sun and observe the highest phase angles. Table 1 summarizes all the images obtained.

The first look was in a pair of images from the C3 encounter, taken on November 9, 1996 (Fig. 1). Here the ring is nearly edge-on and shows a puzzling form, incompatible

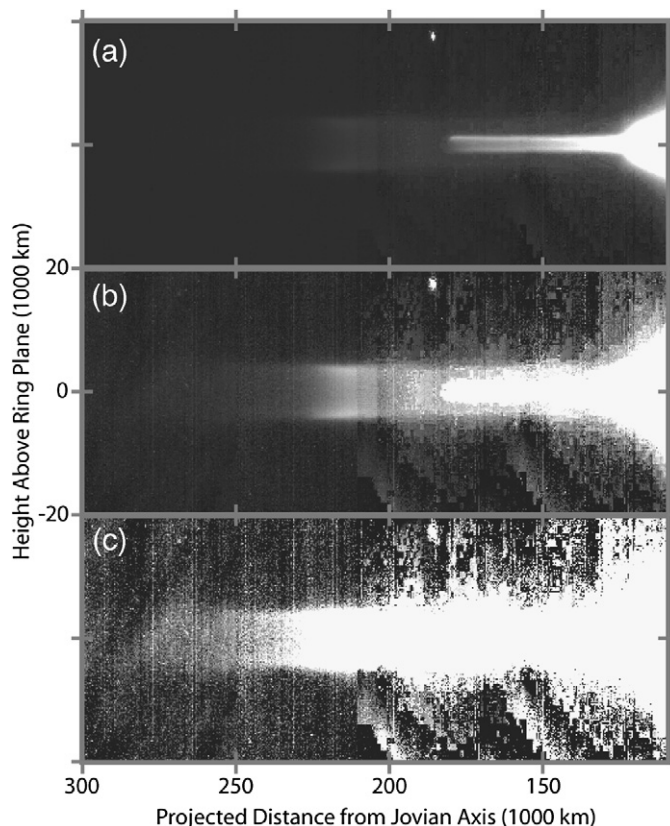


Fig. 2. A mosaic of four edge-on images of the gossamer rings from Galileo's C10 encounter, taken on October 5, 1997. Images C04160889.22–C04160890.45 have been overlaid and expanded vertically by a factor of roughly two (cf. Fig. 1a of Burns et al., 1999). The same mosaic is shown with three different enhancements, each successively showing material fainter by roughly a factor of ten. (a) The main ring and halo are visible at right, with the Amalthea ring extending outward; the Thebe ring is only marginally visible. (b) Thebe's ring is plainly visible. (c) The Thebe ring reveals its outward extension, which matches the thickness of the ring itself in panel (b). The increasing background noise toward the left side of the image is an artifact, due to the decreasing exposure times of the mosaicked frames. The mosaic is oriented with Jupiter's north pole pointed upward. The phase angle ranges from  $177.3^\circ$  at left to  $178.9^\circ$  at right. The ring is open by only  $0.15^\circ$ .

with the flat, equatorial ring that Showalter et al. (1985) had originally assumed. The geometry became clear during the C10 encounter 11 months later, when more extensive imaging was performed. A four-image mosaic shows the edge-on gossamer ring from the main ring's tip out to well beyond the orbit of Thebe. Fig. 2 shows this mosaic in three linear stretches. Here it is oriented with Jupiter's north pole up and celestial east increasing toward the left. [Note that this is rotated  $180^\circ$ , from the orientation shown by Burns et al. (1999).] The borders between individual frames of the mosaic are visible as jumps in the noise level; these occur because the exposure times of the images grow progressively longer from right to left. This set of images revealed the gossamer ring's morphology for the first time, as a set of two vertically extended, overlapping rings, one bounded by Amalthea's orbit and the other by Thebe's (Ockert-Bell et al., 1999; Burns et al., 1999).

Table 1  
Images of the gossamer rings

Data set & image(s)	Number of images	Exposure (s)	Filter	Wavelength ( $\mu\text{m}$ )	Date	Phase angle ( $^\circ$ )	Scattering angle ( $^\circ$ )	Opening angle ( $^\circ$ )	Range (1000 km)	Sun range (AU)	Notes
<i>Voyager 2 Wide Angle Camera</i>											
20693.02	1	15.360	CLEAR	0.35–0.57	1979-07-11	173.76	6.24	1.830	1553	5.33	Gossamer ring discovery image
<i>Galileo SSI</i>											
C03689915.00	1	0.396	CLEAR	0.38–0.82	1996-11-09	178.94	1.06	0.478	2330	5.16	C3RSGOSSMR01
C03689915.22	1	0.529	CLEAR	0.38–0.82	1996-11-09	178.83	1.17	0.478	2330	5.16	C3RSGOSSMR01
C04160731.00/13/20	3	0.063	CLEAR	0.38–0.82	1997-10-05	178.53	1.47	−0.233	6607	5.05	10ESEURPLM01; Europa triple-exposure
C04160731.39/52/59	3	0.396	CLEAR	0.38–0.82	1997-10-05	178.53	1.47	−0.233	6607	5.05	10ESEURPLM01; Europa triple-exposure
C04160764.00/13/20	3	0.096	CLEAR	0.38–0.82	1997-10-05	178.76	1.24	−0.233	6610	5.05	10ESEURPLM02; Europa triple-exposure
C04160764.39/52/59	3	0.529	CLEAR	0.38–0.82	1997-10-05	178.77	1.24	−0.233	6610	5.05	10ESEURPLM02; Europa triple-exposure
C04160889.22	1	0.096	CLEAR	0.38–0.82	1997-10-05	178.89	1.11	0.153	6620	5.05	10RSRINGS_01; Part of edge-on mosaic
C04160889.68	1	0.196	CLEAR	0.38–0.82	1997-10-05	178.50	1.50	0.153	6620	5.05	10RSRINGS_01; Part of edge-on mosaic
C04160890.22	1	0.529	CLEAR	0.38–0.82	1997-10-05	179.58	0.42	0.153	6620	5.05	10RSRINGS_01; Part of edge-on mosaic
C04160890.45	1	0.796	CLEAR	0.38–0.82	1997-10-05	179.58	0.42	0.153	6620	5.05	10RSRINGS_01; Part of edge-on mosaic
C04161101.00/13/20	3	0.096	CLEAR	0.38–0.82	1997-10-06	178.57	1.43	−0.233	6638	5.05	10ESEURPLM03; Europa triple-exposure
C04161101.39/52/59	3	0.529	CLEAR	0.38–0.82	1997-10-06	178.57	1.43	−0.233	6638	5.05	10ESEURPLM03; Europa triple-exposure
<i>Hubble ACS/HRC</i>											
J6MM03DL/M/N	3	450	F814W	0.70–0.95	2003-01-13	4.07		0.029	4.38 AU	5.31	West ansa
J6MM03DO/P/Q	3	285	F606W	0.48–0.71	2003-01-13	4.07		0.029	4.38 AU	5.31	West ansa
J6MM0714/5/6	3	450	F814W	0.70–0.95	2003-02-02	0.16		0.069	4.33 AU	5.31	West ansa
J6MM0717/8/9	3	285	F606W	0.48–0.71	2003-02-02	0.16		0.069	4.33 AU	5.31	West ansa
J6MM09B9/A/B	3	450	F814W	0.70–0.95	2003-02-05	0.61		0.077	4.33 AU	5.31	West ansa
J6MM09BC/D/E	3	285	F606W	0.48–0.71	2003-02-05	0.61		0.077	4.33 AU	5.31	West ansa
<i>W.M. Keck Telescope</i>											
NIRC	115	2300 <sup>a</sup>	CH4	2.190–2.345	1997-08-14	1.07		0.170	4.05 AU	5.06	West ansa
NIRC	110	3000 <sup>a</sup>	CH4	2.190–2.345	1997-08-15	1.28		0.166	4.05 AU	5.06	East ansa
NIRC	70	2000 <sup>a</sup>	CH4	2.190–2.345	1997-10-21	11.02		0.001	4.70 AU	5.04	East ansa
NIRC	125	3200 <sup>a</sup>	CH4	2.190–2.345	1997-10-22	11.07		0.001	4.72 AU	5.04	West ansa
NIRC	107	5580 <sup>a</sup>	CH4	2.190–2.345	2002-12-19	8.22		0.039	4.61 AU	5.30	
NIRC	62	1760 <sup>a</sup>	CH4	2.190–2.345	2003-01-22	2.32		0.042	4.34 AU	5.34	

<sup>a</sup> For Keck images, only the total integration time per night is listed. Exposure times for individual images varied from 10 to 90 s.

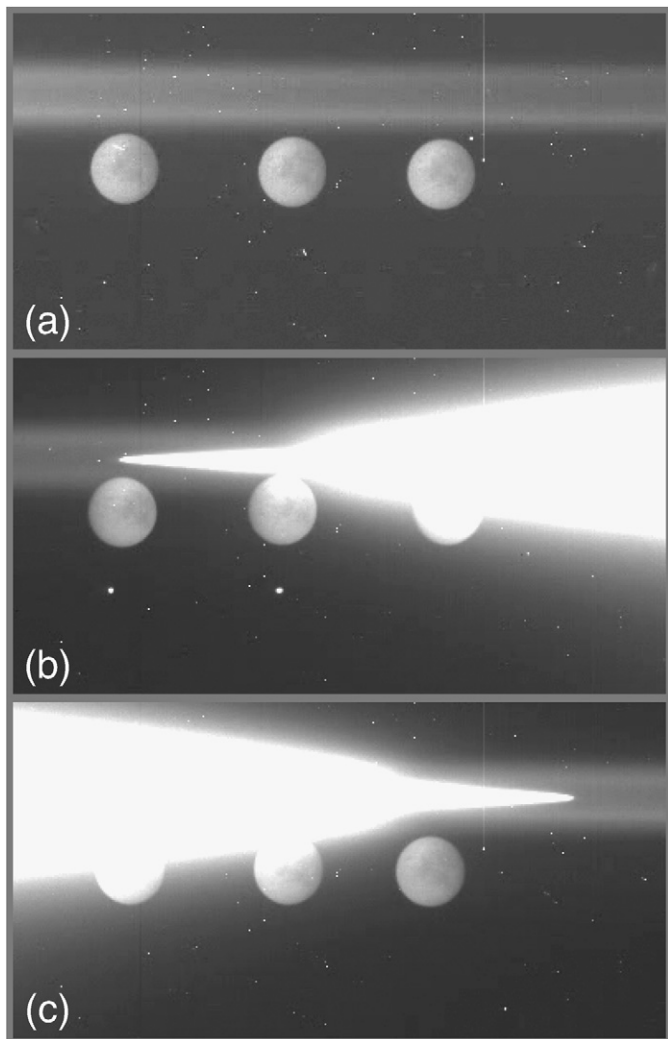


Fig. 3. A striking set of Europa images from the C10 encounter, taken October 5–6, 1997. The images are triple-exposures of the dark side of Europa, illuminated by light reflected from Jupiter. The ring system (excluding the Thebe ring, which is too faint) are visible just north of the satellite. (a) Images C04160731.00–C04160731.20; (b) images C04160764.00–C04160764.20; (c) images C04161101.00–C04161101.20.

The C10 encounter produced an additional, visually striking set of gossamer ring images. A sequence imaged the dark side of Europa, illuminated exclusively by light reflected off Jupiter. The images also captured the (sometimes over-exposed) main ring and halo with the Amalthea ring extending outward (Fig. 3). The images were triple-exposures, each containing three images of Europa and therefore three overlapping, radially shifted images of the rings. This makes any detailed geometric or photometric interpretation of the images challenging. However, as will be shown below, they still provide useful information about the ring's vertical structure.

The Galileo images were calibrated using a standard procedure called “GALSOS.” The resultant images are in units of  $I/F$ , where intensity  $I$  has been scaled to  $F$ , defined such that  $\pi F$  is the incoming solar flux. This convenient quantity is dimensionless and has the solar spectrum removed. It is equal to the geometric albedo for a perfectly diffusing “Lambert” sur-

face oriented normal to the sunlight. The images were obtained through Galileo's clear filter, which has a broad bandpass of 0.38 to 0.82  $\mu\text{m}$ , centered on 0.611  $\mu\text{m}$ .

## 2.2. HST images

An unusual Earth-based observing opportunity occurred on December 2002–February 2003, when the rings of Jupiter swept through nearly their full range of phase angles while remaining nearly edge-on to Earth; the ring opening angle stayed below  $0.07^\circ$  during this entire period. As the Galileo images aptly illustrate, edge-on viewing geometries are optimal for detecting and studying faint, dusty rings. Showalter et al. (2003) carried out observations of the jovian ring system using the Advanced Camera for Surveys (ACS) on the Hubble Space Telescope. ACS's High Resolution Camera (HRC) has a pixel scale of  $0.025''$  per pixel, corresponding to 75 km at Jupiter's opposition distance. The point spread function is just a few times larger. Showalter et al. carried out ten “visits” to Jupiter—seven targeted at the main ring and three at the Amalthea ring. The HRC's  $25''$  field of view is sufficient to encompass the main rings or the Amalthea ring but not both. (Estimates of instrument sensitivity indicated that the Thebe ring would not be detectable within reasonable integration times.) Each visit lasted a single HST orbit, allowing for  $\sim 50$  min of uninterrupted imaging. Visits were carefully timed to exclude all jovian moons except the two innermost ring moons, Adrastea and Metis. Our results on the main ring are discussed elsewhere (Showalter et al., 2003, 2005).

The Amalthea ring was imaged using two broadband filters F606W and F814W, roughly equivalent to standard filters V and I. The three visits captured phase angles  $\alpha = 0.16^\circ$ ,  $0.61^\circ$  and  $4.07^\circ$ ; these were chosen to search for an opposition surge, which is a non-linear increase in brightness near backscatter (typically phase angle  $\alpha < 1^\circ$ ), often observed on rough bodies.

Very long integrations were required to detect Amalthea's ring (Table 1); had Jupiter been inside the field of view, it would have been overexposed by a factor of  $\sim 400$ . It is a testament to the design of the ACS optics that these images were not saturated by off-axis scattered light from the planet (Fig. 4a). The integration time was split between three images through each filter; each triplet was then median-filtered (Fig. 4b) to eliminate cosmic ray hits, which can be particularly severe in long integrations. Finally the gradient in background light has been modeled by a third-order, two-dimensional polynomial. Upon subtraction, it leaves behind a clear view of the Amalthea ring (Fig. 4c).

The HRC images are calibrated as follows. CCDs create images by converting photons into electrons. Calibrated HRC images are provided in units of the number of electrons accumulated in each pixel. The image labels include a parameter PHOTFLAM, which converts from electrons per second to physical units of  $\text{erg cm}^{-2} \text{\AA}^{-1}$  (Pavlovsky et al., 2005). To convert to  $I/F$ , we need a corresponding value for the Sun's incoming flux density  $\pi F$  as measured at 1 AU. This is generated by convolving the bandpass of the filter and electronics with

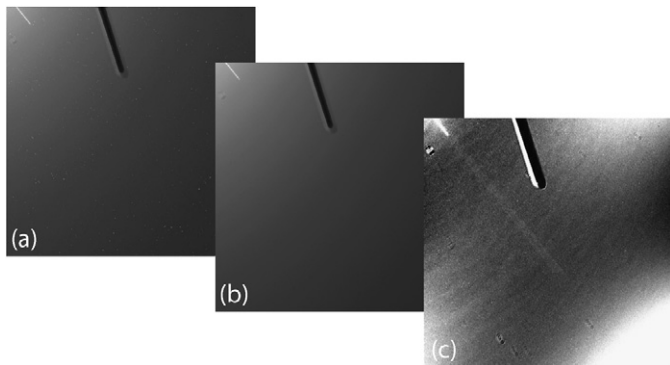


Fig. 4. A sample image of Amalthea's ring from the Advanced Camera for Surveys on HST. Shown are images taken through filter F606W during Visit 07; see Table 1 for details. (a) Single image J6MM03DO, showing the tip of the main ring at upper left. The large brightness gradient from upper left to lower right is scattered light from the nearby planet. Numerous cosmic ray hits are visible as white spots. The black bar near top center is the mount for ACS's occulting mask. (b) The cosmic ray hits have been removed by selecting the median pixels from the three images taken with the same filter during this visit. (c) A third-order polynomial has been fitted to the image and subtracted. The Amalthea ring is now plainly visible.

the solar spectrum (American Society for Testing and Materials, 2000). From this information, the conversion factor from electrons to  $I/F$  is

$$I/F \text{ per } e^- = \text{PHOTFLAM} \bullet R_{\text{Sun}}^2 / (T_{\text{exp}} \bullet \Omega_{\text{pixel}} \bullet F), \quad (1)$$

where  $R_{\text{Sun}}$  is the distance from the Sun to Jupiter in AU,  $T_{\text{exp}}$  is the exposure time in seconds, and  $\Omega_{\text{pixel}} \approx 1.647 \times 10^{-14}$  is the area of a pixel in steradians (Pavlovsky et al., 2005). We analyze images that are calibrated but not geometrically corrected (designated "FLT"), so we must allow for the distortion in our analysis. For this purpose we employ a fourth-order polynomial to convert between pixel coordinates and sky coordinates (Anderson and King, 2004). Because of this distortion, pixel areas  $\Omega_{\text{pixel}}$  vary by a few percent across the HRC's field of view; however, we ignore this small correction to our photometry.

### 2.3. Keck images

Using the 10-m W.M. Keck I telescope<sup>1</sup> on Mauna Kea, Hawaii, we observed Jupiter's ring system during its edge-on appearances in August and October, 1997 (Fig. 5) and again in December 2002–January 2003. The images from August 1997 were published by de Pater et al. (1999); here we present additional data taken on UT October 21 and 22 (Table 1). The planet's phase angle was  $\alpha = 11.0^\circ$ , in contrast to the August data taken near opposition at  $\alpha = 1.1^\circ$ . De Pater et al. (2008) present further details of the 2002–2003 data; here we use their more recent data only to augment the gossamer ring's phase curve.

We obtained the data with the facility's near-infrared camera (NIRC; see Matthews and Soifer, 1994), which is equipped

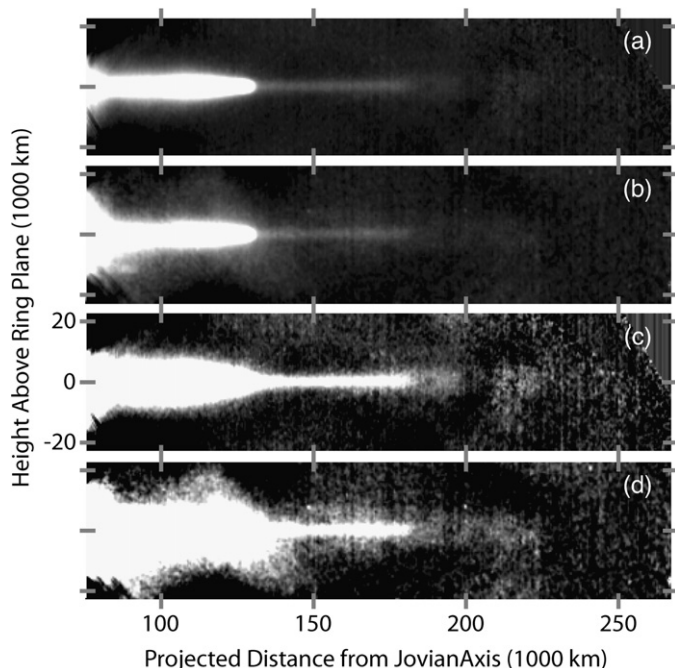


Fig. 5. Coadded images from the Keck Telescope of the edge-on jovian ring system from (a) August and (b) October 1997 show the Amalthea ring extending outward from the main ring and halo at left. The same images are enhanced further in panels (c) and (d) to show the Thebe ring more clearly. Interference from moons left a dark gap in the August image of the Thebe ring (c), but the October image (d) is much freer from interference.

with a  $256 \times 256$  pixel InSb array from Santa Barbara Research Corporation. The pixel size is  $0.151''$ , corresponding to 516 km at Jupiter. All observations were conducted in the CH4 filter, which is centered at a wavelength  $\lambda = 2.27 \mu\text{m}$  (2.190–2.345  $\mu\text{m}$ ). Sunlight, usually reflected by Jupiter's thick cloud layers, is absorbed at this wavelength by methane gas above the main cloud deck, making the planet very dark and greatly reducing scattered light near the rings. The seeing was  $\sim 1''$  (3400 km at Jupiter) on October 21 and  $\sim 0.7''$  (2400 km) on October 22.

We observed the east side of Jupiter's ring on 21 October and the west side on 22 October. These dates and sides were carefully chosen to avoid appearances by the Galilean moons. Observational sequences contained five images of Jupiter's ring, dithered in position to avoid superposition of bad pixels. Sky frames were taken between sets of ring images. The data were linearized and flat-fielded according to standard procedures (Graham et al., 1994). The absolute calibration of the images was set by observing the HST IR standard stars SJ9182, FS34 and P247, which have K-band ( $\lambda = 2.24 \pm 0.23 \mu\text{m}$ ) magnitudes of 11.082, 12.989, and 11.492, respectively (Persson et al., 1998) and adopting 646 Jy as the flux density from a zero-magnitude star. (Recall that  $1 \text{ Jy} = 10^{-26} \text{ W m}^{-2} \text{ Hz}^{-1}$ ). We measured the extinction coefficient for each night by observing the standard stars over a range of airmasses. At one airmass, one count/s corresponded to a flux density of  $0.155 \mu\text{Jy}$  on each night. The extinction coefficients were 0.07 and 0.1 magnitudes per airmass on October 21 and 22, respectively. Stellar observations suggest that our calibration uncertainty is  $\sim 3\%$ .

<sup>1</sup> The W.M. Keck telescopes are jointly owned and operated by the University of California and the California Institute of Technology.

Because the seeing on 22 October was much better than on the night before, we focus here on that data set. Amalthea and Thebe interfered with the August observations, so the October image shows the outer part of the gossamer rings much more clearly (Fig. 5d). For example, as expected, the Thebe ring shows a more uniform radial profile, without the anomalous dip in the intensity that was seen in the August data (Fig. 5c; cf. Fig. 3 of de Pater et al., 1999).

To compare our measurements with previous results and physical models, we convert from units of Jy per pixel to  $I/F$ . Integrating the infrared solar spectrum of Colina et al. (1996) over the narrow CH<sub>4</sub> bandpass, we derive a solar flux  $\pi F = 1.264 \times 10^{14}$  Jy at 1 AU. For an image value  $DN$  in Jy/pixel, we have

$$I/F = DN \cdot R_{\text{Sun}}^2 \cdot \pi / (\Omega_{\text{pixel}} \cdot 1.264 \times 10^{14}). \quad (2)$$

The pixel scale  $\Omega_{\text{pixel}} = 5.36 \times 10^{-13}$  so, for a nominal  $R_{\text{Sun}} = 5.20$ ,  $I/F$  per  $DN = 1.25$ . However, we have incorporated the correct Sun–Jupiter distance into our calibration for each observing period.

#### 2.4. Voyager image

Voyager’s single discovery image has been discussed and analyzed previously (Showalter et al., 1985). However, because it complements the high-phase imaging by Galileo (Table 1), we include it in this study. It has been calibrated and geometrically corrected using time-honored procedures; absolute calibration in units of  $I/F$  should be accurate to  $\sim 5\%$ . Voyager’s vidicon did not respond to long wavelengths of light, so the passband of its clear filter was very different than that of Galileo; it peaked at  $0.44 \mu\text{m}$  and had a full range from  $0.30$  to  $0.62 \mu\text{m}$ .

### 3. Photometric modeling

The variation in ring brightness with phase angle places strong constraints on the particle size distribution within a dusty ring. The jovian main ring has been studied repeatedly in this manner (Showalter et al., 1987; McMuldroy et al., 2000; Porco et al., 2003; Brown et al., 2003; Throop et al., 2004; Brooks et al., 2004).

However, photometry of the gossamer rings has never been performed, due to a dearth of data with high signal-to-noise ratio (SNR). As Table 1 indicates, we have assembled here data spanning the highest and lowest phase angles, which are the ones most diagnostic of particle sizes. By combining all the available data, reasonable inferences about the dust size distribution become possible. Much of our data is in the visual through nominally clear filters, reducing the possibility that ring color has biased our measurements significantly.

#### 3.1. Measurement procedure

Because the rings are diffuse clouds with varying structure, obtaining reliable ring photometry remains difficult. Intensity varies with viewing geometry, because each image pixel integrates a distinct line of sight through the cloud. Therefore, it

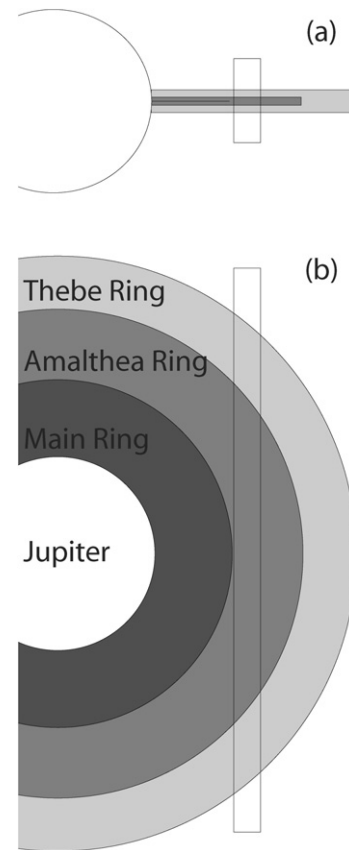


Fig. 6. A diagram illustrating the ring region that has been integrated for our photometry. (a) The box shows a region crossing the ring system vertically and spanning projected distances of 130,000 to 150,000 km from Jupiter’s rotation axis. This same region is visible in nearly all of our images, so consistent photometry can be obtained by generating a vertical profile of  $I/F$  across the ring and integrating the area under the curve. The Thebe ring’s contribution is subtracted out of these profiles when it is visible, by extrapolating its brightness as measured from regions above and below the Amalthea ring. Thus our photometry refers exclusively to Amalthea’s ring. (b) A top view shows the area of the ring contained in our integration box.

is difficult to decouple the variations due to phase angle from those due to geometry.

Nevertheless, we have identified one region of the ring that is seen consistently in every data set. It is a swath of the Amalthea ring seen spanning the projected range 130,000 to 150,000 km, which is just off the tip of the main ring (Fig. 6). In practice, this selected region is strongly biased toward the innermost portions of the ring; however, the figure shows that outer regions are also sampled, but weighted less heavily, in the region selected. Regardless of the ring’s three-dimensional form, if we integrate over the equivalent set of particles in each of our measurements, the dependence on viewing geometry is eliminated. Note that the ring is very optically thin so that mutual shadowing is negligible; we can always see every dust grain. It is helpful that this region is also rather bland and uniform, meaning that we can safely adjust the radial limits slightly as is demanded by individual data sets. In particular, the inner limit had to be adjusted upward to 132,000–135,000 in some Earth-based images to ensure that light from the main ring did not enter into our measurement.

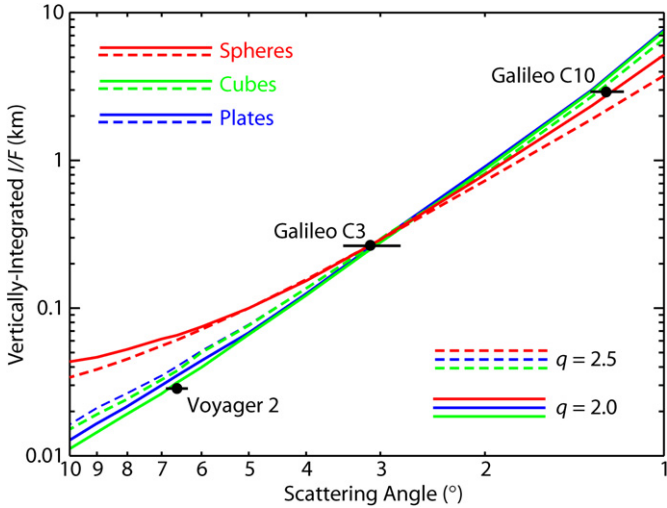


Fig. 7. Phase curve of the Amalthea ring at high phase angles, based on Galileo and Voyager images. The three plotted points are vertically-integrated  $I/F$  values derived from the ring region between projected radii of 130,000 and 150,000 km (Fig. 6). Measurement uncertainties are  $\sim 6\%$ , comparable to the sizes of the points shown. The points are plotted against scattering angle, the supplement of the phase angle. Horizontal bars indicated the range of scattering angles averaged for each measurement. Model phase functions are also shown for comparison. These models correspond to broad power laws with indices of 2 (solid lines) and 2.5 (dashed lines); this range appears to encompass the best fits to the data. Various shape models are also considered: red for spheres, green for irregular cube-like particles and blue for plate-like particles. The models have been scaled to pass through the Galileo C3 measurement near  $3^\circ$ . All models fit the Galileo C10 measurement but only the irregular particles provide a reasonable fit to the Voyager measurement.

To obtain each measurement, we generate a profile vertically across the ring, in which pixels at a common distance above or below the ring plane are averaged together. By using a broad radial range, we smooth out some of the noise and local variations in each image, yielding a higher SNR. Each resulting profile shows the ring's edge-on  $I/F$  versus elevation  $z$  above the ring plane. We then “flatten” each profile by fitting a low-order polynomial to the regions above and below the Amalthea ring; this eliminates any underlying brightness gradients and also removes the Thebe ring from those images in which it is detectable. We then integrate the area under this curve to produce a “vertically-integrated  $I/F$ ” in units of meters or km. One advantage of this integrated quantity is that it is independent of resolution—at lower resolution the ring profile is thicker but the height of the curve is reduced correspondingly, so that the area is conserved. Variations of ring opening angle among the profiles play a completely negligible role.

### 3.2. High-phase photometry

Micron-sized particles preferentially diffract light into a forward-scattering cone of width  $\Delta\theta \sim \lambda/2\pi a$ , where  $\theta \equiv 180^\circ - \alpha$  is the scattering angle,  $a$  is the particle radius, and  $\lambda$  is the wavelength of the light. For this reason, the highest phase angles are most diagnostic of particle sizes within a dusty ring.

The Voyager and Galileo high-phase measurements are shown in Fig. 7. Statistical uncertainties are  $\sim 6\%$ , compara-

ble to the size of the dots plotted. The background level is the largest contributor to this uncertainty; this background must be subtracted from each vertical ring profile prior to the integration. Our estimates are based on the deviation among various models fitted to the sky region surrounding the ring. An additional systematic uncertainty of  $\sim 5\%$  may arise from possible errors in the relative calibration of the Voyager and Galileo cameras.

In the figure, the three points are compared to a set of models using power-law size distributions. Power laws have the simple form  $n(a) \sim a^{-q}$ , where  $n(a)$  is the differential size distribution, defined such that  $n(a) da$  is a number of particles between  $a$  and  $a + da$ . Here  $q$  is referred to as the “power-law index.” In addition to their overall simplicity, power-law models are preferred because many astrophysical ensembles of particles obey such laws (Dohnanyi, 1972).

In Fig. 7, models are shown for power law indices of 2 and 2.5. We have experimented with  $q$  in the range 1 to 6 in steps of 0.5, but the overall best fits fall within this narrow range. The integration limits used for this model are  $a = 0.001$  to  $100 \mu\text{m}$ , but we find that curve's shape depends little on the precise limits chosen. Because of the high scattering angle, the phase curve primarily constrains particles in the size range  $4\text{--}30 \mu\text{m}$ .

We must also assume a refractive index to generate the curves. We have used olivine and pyroxene as representative of the ring material. The refractive index in the visual is  $m \sim 1.64 - 0.0002i$  (Pollack et al., 1994). The refractive index, particularly its imaginary component, varies with wavelength, so we have generated phase function models for small steps in wavelength and then integrated these across the bandpass of each instrument/filter combination. However, in practice, we find that the phase function models are nearly independent of the details of each visual-band observation.

The figure shows three different models for particle shape: spheres, cubes and plates. The spherical model is derived from Mie Theory; the cube and plate models are based on the semi-empirical model of Pollack and Cuzzi (1980); cf. Showalter et al. (1992). Although far more sophisticated (but computationally intensive) models for irregular particle shapes exist today, we find in practice that the Pollack and Cuzzi model is generally adequate for our purposes, particularly for observations at low and high phase angles. The largest discrepancies occur at intermediate phase angles, where observations of the gossamer rings are absent.

Because diffraction dominates at the highest phase angles, the phase function models shown in Fig. 7 are not strongly dependent on shape. All the shape models are capable of fitting the two Galileo measurements at the highest phase angles. Nevertheless, the irregular models are significantly better at simultaneously fitting the Voyager measurement at a slightly lower phase angle. In fact, *no* model involving spheres alone was ever able to match all three measurements. So the data suggest that the particles are irregular in shape, which is perhaps not surprising given their likely collisional origins. Throop et al. (2004) have also ruled out spherical grains in the main jovian ring.

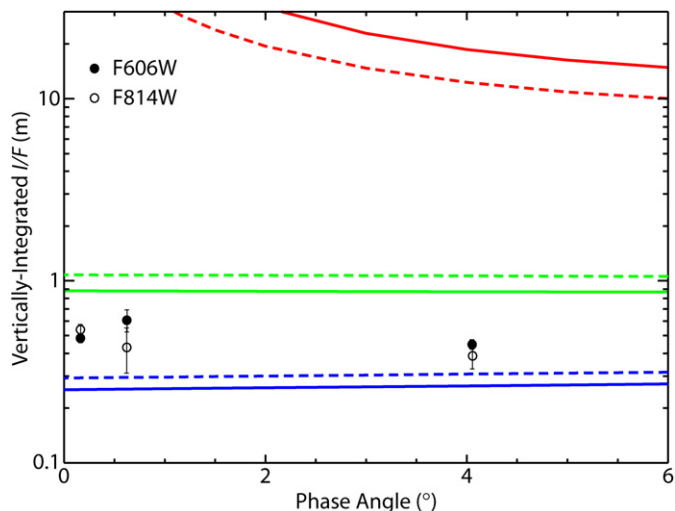


Fig. 8. The backscatter phase curve of the Amalthea ring is shown from HST ACS data. Solid circles indicate the F606W measurements and open circles indicate the F814W measurements. Vertical error bars indicate  $\pm$  one standard deviation. Somewhat unexpectedly, the ring shows no strong variation with either phase angle or wavelength. For comparison, the phase curves defined in Fig. 7 have been extended into the backscatter regime and are shown here. Spherical particle models (red) provide a poor fit to the data but irregular particles (blue and green) appear to span the range of measurements obtained. These models are almost flat near backscatter, providing a natural explanation for the absence of a significant slope to the measurements.

### 3.3. Low-phase photometry

Fig. 8 shows the Amalthea ring's backscattering phase curve, as derived from the ACS images. The ring has a somewhat unexpected property that the curve is essentially flat. This is unusual; virtually all rings and certainly all moons exhibit a brightening trend toward zero phase. Throop et al. (2004) and Wong et al. (2006) report that the main ring's phase curve is nearly flat near backscatter, but Showalter et al. (2005) find a modest brightening in the main ring, by 30–50% at phase angles below  $\sim 5^\circ$ .

However, the figure also shows the same three photometric models as in Fig. 7, now extrapolated to backscatter but still scaled to fit the high-phase measurements. The Mie model has a backscattering “glory” and extends off the top of the figure; this feature is most definitely not seen in the data. However, the irregular models predict a flat phase curve in backscatter. Furthermore, the models for cubes and plates straddle the backscattering measurements. Thus, while neglecting the details of the particle shape, we can assert that all the available photometry is consistent with irregular grains obeying a power-law size distribution with  $q = 2\text{--}2.5$ . Power law indices outside this range show very different slopes that are incompatible with the data.

We also have infrared data from the Keck telescope near backscatter; it is compared to the visual data from ACS in Fig. 9. The Keck measurements confirm the flat backscattering phase curve of the Amalthea ring. However, they are also brighter than the ACS data by a factor of  $2.8 \pm 0.3$ . For the ring to have a red color should not be surprising, given that all of Jupiter's inner moons and rings are red (Gradie et al., 1980; Showalter et al., 1987; Thomas et al., 1998; de Pater et al., 1999;

Throop et al., 2004). However, the meaning of a ring's color is not so simple when it is composed exclusively of dust. In this case, the particle size and shape can significantly alter the color of the ring. For example, the E ring's well-known blue color is the result of its fine particle sizes, not some intrinsically blue coloration of the ring material (Showalter et al., 1991; Nicholson et al., 1996). Throop et al. (2004) find that the main jovian ring is also red, although larger bodies contribute about half of its backscattered intensity.

The general rule is that steep size distributions (i.e., large  $q$ ) tend to appear blue because the smallest particles dominate, and they reflect shorter-wavelength blue light more efficiently than red. For flatter distributions (small  $q$ ) the larger sizes dominate so the color is redder. Showalter et al. (1987) used very simple arguments to show that a ring's wavelength dependence should be roughly proportional to  $\lambda^{3-q}$ . The wavelengths of the Keck and ACS data sets differ by a factor of  $\sim 3.2$ , so a color ratio of  $2.8 \pm 0.3$  implies  $q = 2.1 \pm 0.1$ . Thus, the ring's color in backscatter provides independent support for the derived power law size distribution. It should be acknowledged, however, that this same spectral slope ought to reveal about a 30% brightening between the two ACS filters F606W and F814W; this is not observed, perhaps simply because the error bars on individual measurements are relatively large.

Burns et al. (1984) note that impact debris commonly obeys a power law with  $q \sim 3.4$ . However, drag forces operate on smaller grains faster than large ones; this has the effect of reducing  $q$  by unity, to  $q \sim 2.4$ . The close match between this theoretically-derived index and the observed value lends support to the model of gossamer ring dust arising as impact ejecta from Amalthea and Thebe and evolving inward under PR drag.

## 4. Three-dimensional structure

Burns et al. (1999) posit that the gossamer rings are composed of dust grains that have been ejected off the surfaces of Amalthea and Thebe by meteoroid impacts. The grains then evolve inward under PR drag. From this model we can make very simple mathematical predictions about the three-dimensional structure of the two rings. Here we derive this 3-D model and test it quantitatively against the observations.

### 4.1. Ring model

Let us describe the local amount of ring material in one of the gossamer rings by a function  $n$ , such that  $n(a, r, \phi, z) da$  is the number of particles of radius  $a$  to  $a + da$ , at a location defined by standard cylindrical coordinates  $(r, \phi, z)$ . The model predicts no longitudinal asymmetries, so we eliminate the  $\phi$ -dependence immediately.

Dust with a particular size distribution is ejected from the surface of Amalthea or Thebe and then begins its journey inward. Small grains evolve faster than large ones under PR drag, so the local ring population might be depleted in the smallest grains relative to the source population. As noted above, the effect of a drag force is to reduce the power-law index  $q$  by one (Burns et al., 1984). Regardless, the model predicts that each

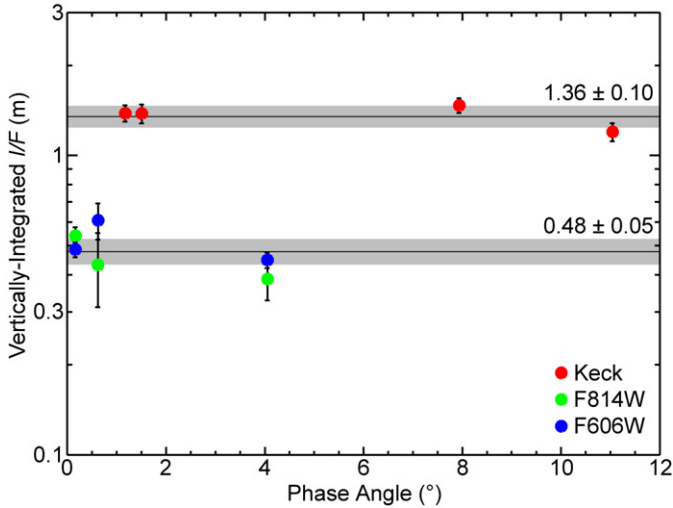


Fig. 9. The phase curve near backscatter is shown for measurements at three wavelengths, 0.6  $\mu\text{m}$  (ACS F606W), 0.8  $\mu\text{m}$  (ACS F814W), and 2.2  $\mu\text{m}$  (Keck). Vertical error bars indicate  $\pm$  one standard deviation. The ring is much brighter in the infrared. Horizontal lines and gray bars indicate the mean and  $\pm$  one standard deviation from the Keck and ACS measurements.

grain evolves inward at a fixed rate, provided its size remains constant. Thus, the form of the ring's size distribution should be independent of location. This enables us to separate variables, yielding

$$n(a, r, z) = n(a)h(r, z), \quad (3)$$

where  $n(a)$  describes the particle sizes as above and  $h(r, z)$  describes the ring's radial and vertical structure.

Suppose the source body orbits at semimajor axis  $r_0$  with inclination  $i_0$ . Under the action of PR drag alone, dust grains will conserve their orbital inclinations as they evolve inward. This defines the half-thickness of each ring,

$$z_{\text{max}}(r) = r \sin(i_0) = (r/r_0) \cdot z_0, \quad (4)$$

where  $z_0$  is half the vertical extent of each moon's motion. The parameter values are  $(r_0, z_0) = (181,300 \text{ km}, 1260 \text{ km})$  for Amalthea and  $(221,000 \text{ km}, 4130 \text{ km})$  for Thebe (Burns et al., 2004). Note that, according to this relationship, the ring's local thickness will shrink in proportion to  $r$  as grains evolve inward. Here we have neglected the eccentricity of each moon, which makes the outer edge of each ring less abrupt as noted by Burns et al. (1999).

The nodes of the orbits spread rapidly after their ejection from the source moons, so each ring is not an inclined disk but the thick, cylindrical structure observed. Particles on inclined orbits spend more of their time near the vertical extremes of their motion, so the ring will be denser near its northern and southern limits. The vertical dependence can be readily shown to obey this relationship:

$$h(r, z) \propto (1 - (z/z_{\text{max}})^2)^{-1/2}. \quad (5)$$

This arises from the fact that local density is inversely proportional to the vertical velocity of a particle. Horanyi et al. (1992) investigated the theoretical radial profile of a dusty ring and found a functional form analogous to Eq. (5). This function

diverges at  $z = \pm z_{\text{max}}$ , because the vertical motion is instantaneously zero at its extremes. However the area under the curve as a function of  $z$  remains finite. A more accurate model for  $h(r, z)$  would not diverge because  $z_{\text{max}}$  is not a constant; rather, it is the mean of a narrow size distribution, whose width is defined by the physical size of the source moon and by the variations in the initial ejection velocity. A more accurate model could be created by superimposing a family of models in which  $z_{\text{max}}$  is suitably randomized, but the difference would be negligible. In practice we retain the simple model above but cap  $h(r, z)$  at a value  $\sim 10$ . This cutoff affects the upper and lower 0.5% of the ring's vertical thickness and eliminates  $\sim 3\%$  of the ring's particles. This computational precision is quite adequate for our purposes.

Because grains evolve inward at a nearly uniform rate, the number of particles residing in any concentric cylindrical shell of the same radial width is conserved. This means that the local density of particles increases as  $1/r^2$ , due to the simultaneous decrease in orbital radius and in  $z_{\text{max}}$  [Eq. (4)] as orbits evolve inward. Combining these formulas yields the overall, predicted 3-D model for the ring:

$$h(r, z) = (r_0/r)^2 (1 - (z/z_0 \cdot r_0/r)^2)^{-1/2}, \quad (6)$$

which has been normalized arbitrarily so that  $h(r_0, 0) = 1$ .

Fig. 10 illustrates the model, showing both cross-sectional and edge-on views of a hypothetical ring. Because  $h(r, z)$  can be readily integrated along any line of sight, we can use it to create pseudo-images that match the geometry of any existing image. We generate these pseudo-images by numerically integrating the function along the line of sight of every pixel, using the same viewing geometry and field of view of the corresponding image. The function is evaluated at 100-km steps, a distance that was found to provide a reasonable balance between numeric precision and computational speed. Burns et al. (1999) used this same technique, and the same formula, for their Fig. 2, which is a pseudo-image used for comparison to their data. With the complete set of pseudo-images in hand, we are now prepared to quantify the comparison between the images and the model.

Of the limited available data, the C10 mosaic shows most clearly the radial and vertical structure of these two rings. Superficially, it reveals all the key features predicted by the model. Each ring is bounded at its outer edge by the orbit of its source moon, and has a vertical thickness that closely matches the expected value of  $z_{\text{max}} = r_0 \sin(i_0)$ . Also, each ring shows the expected concentrations of material near its upper and lower extremes. These features can be seen by a comparison of Figs. 2 and 10; see also Figs. 1a and 2 of Burns et al. (1999). The outermost boundary of each ring is not as abrupt as the model predicts, but this is easy to understand as blurring caused by each moon's orbital eccentricity, which was neglected in this model.

#### 4.2. Radial profiles

The simplest comparison to make between the images and the models is via vertically-integrated radial profiles of the rings. As with our photometric modeling above, the measured

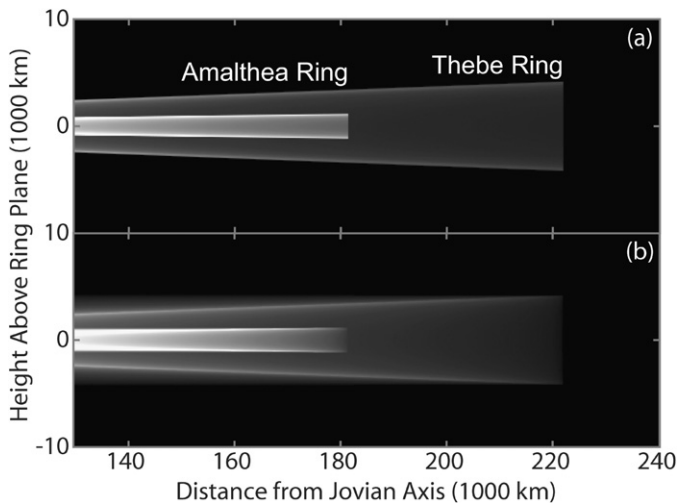


Fig. 10. Synthesized images of the gossamer rings. The overlapping Amalthea and Thebe rings are shown in (a) cross-sectional and (b) edge-on views (cf. Fig. 2 of Burns et al., 1999). For this figure the density functions  $h(r, z)$  have been scaled so that both rings have the same normal optical depths; the Thebe ring is fainter overall here only due to its greater vertical thickness. The images have been expanded vertically by a factor of two to better show the rings' predicted vertical structure.

quantity is the area under the curve of  $I/F$  as a function of height  $z$  above the ring plane. However, here we plot that quantity as a function of projected radial distance from the center of Jupiter. Fig. 11 shows profiles of the Amalthea and Thebe rings derived from the images of Galileo's C10 mosaic. For Amalthea's ring (Fig. 11a) we plot the northern and southern halves of the ring separately to investigate the ring's north-south asymmetry. For both rings, the comparison between the measured profiles and the predictions is less than satisfactory. The model predicts rings that arise at the orbit of each moon but grow in brightness only gradually with decreasing projected radius. For comparison, the observed profiles show sharper rises near their outer tips and then a flatter profile inward from there. This difference requires an excess of material near the outer limit of each ring. However, aside from this regional discrepancy, the models and the profiles show reasonable agreement. Inward of 160,000 km in Amalthea's ring and inward of 185,000 km in Thebe's ring, the models and measurements show similar shapes. This suggests that, inward from these localized peaks, the rings are more uniform and the model fits the data reasonably well.

Fig. 12 shows the Amalthea ring in backscattered light from ACS data. Here the fit is less successful. The edge-on ring is nearly uniform in brightness whereas the model predicts the slow, steady increase toward lower projected radii. Although the Keck profile has not been shown here, its shape is very similar to that seen in the ACS data (de Pater et al., 1999). The form of, and implications of, this discrepancy will be discussed further below.

Reasoning by analogy to the Thebe ring and its outward extension, one might ask whether Amalthea's ring also has a faint component extending outward from its tip. Thebe's outward extension conserves the ring's thickness but is only about  $\sim 10\%$  as bright. Any analogous extension of Amalthea's ring would

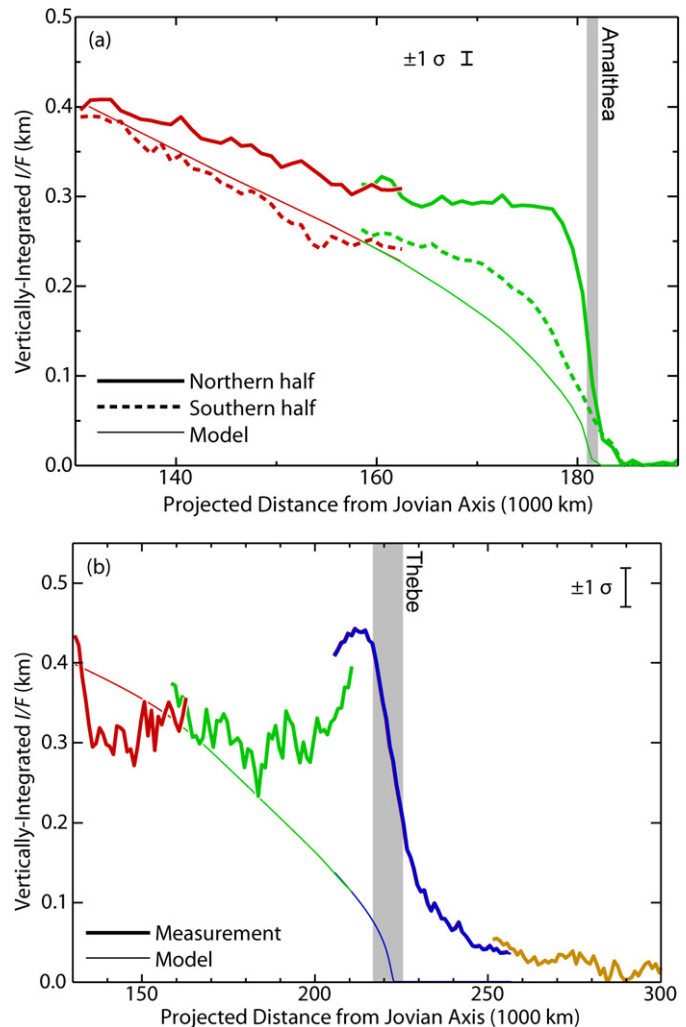


Fig. 11. Measured edge-on radial profiles of (a) the Amalthea ring and (b) the Thebe ring, derived from Galileo's C10 mosaic, are compared to the model. Segments corresponding to the four images are identified by color: red for C0416088922, green for C0416088968, blue for C0416089022, and orange for C0416089045. Thick lines indicate measurements and thin lines indicate model profiles based on the given viewing geometry of each individual image. Statistical error bars of  $\pm$  one standard deviation are shown; possible systematic uncertainties related to the background level are comparable. The model curves have been generated by integrating synthetic images and then smoothing slightly to reduce variations caused by the finite sampling steps in the numeric integrations. The models have been scaled arbitrarily to foster comparison to the data. Amalthea's ring has been divided into northern (solid line) and southern (dashed line) halves to better reveal the vertical asymmetry. Both rings show a marked excess of material near their outer tips. The radial extremes of each source moon's motion are indicated with vertical gray bars.

be visible overlaying the Thebe ring and about equal to it in brightness. A search for material matching the thickness of the Amalthea ring but outside Amalthea's ring has been negative, providing an upper limit of a few percent of the ring's brightness. Thus, the outward extension to the Thebe ring has no clear analog in Amalthea's ring.

#### 4.3. Vertical structure

It is also informative to compare the rings' vertical structure to the model. The presence of brightness peaks near the ver-

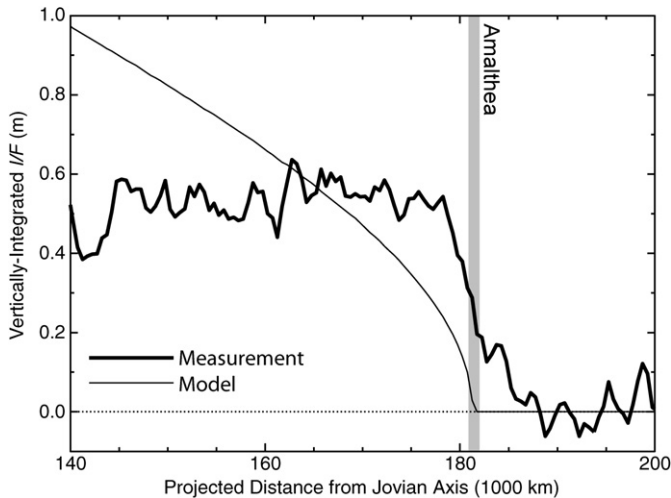


Fig. 12. A measured profile of the Amalthea ring from all the combined ACS data is shown for comparison with the model. The radial limits of Amalthea's eccentric motion are indicated by a vertical gray bar. The heavy line indicates the ring's measured, edge-on intensity; whereas the light line indicates the model. The model has been smoothed slightly and scaled arbitrarily for easier comparison to the data. The data and the model are clearly incompatible.

tical extremes of each ring was a strong driver behind Burns et al.'s (1999) proposal that inward-evolving dust grains preserve their inclinations. One consequence is that the ring should narrow with decreasing radius, which has already been noted (Burns et al., 1999; de Pater et al., 1999). Fig. 13 provides a more detailed comparison; it shows a sequence of vertical profiles across the rings from the C10 mosaic images. In each case the measured profile is compared to an identical profile as obtained from a pseudo-image that matches the viewing geometry and resolution, derived by integrating the 3-D model along each pixel's line of sight. Amalthea's ring shows a very close alignment between the predicted and observed peaks, indicating that the mean inclination of the dust particles is conserved. However, the peaks themselves tend to be broader and less sharp, indicating that initial inclinations are distributed narrowly about their predicted mean. The non-zero launch velocities of grains from the source moons undoubtedly contribute to this effect; however, this result may also indicate that the particles respond to small vertical perturbations during their journeys inward.

The Thebe ring's profile is less compatible with the model, indicating that its grains have a broader distribution of inclinations. Furthermore, the peaks become distinctly less sharp in the inner Thebe ring (compare Figs. 13c and 13d), suggesting that in this case the distribution of inclinations is broadening during the journey inward. Particles derived from Thebe cross the strong 3:2 and 4:3 exterior Lorentz resonances at 209,500 and 193,400 km, respectively, on the journey to the locations shown in Figs. 13b and 13c (Burns et al., 2004, see their Fig. 11.14); kicks received on these passages will increase inclinations. Apparently as a result, Fig. 13b shows that a small amount of the Thebe ring's material is detectable at least 6000 km from the ring plane, well beyond what the model would predict. By contrast, the outward extension to Thebe's ring is no broader than the ring itself (compare Figs. 13d and 13e).

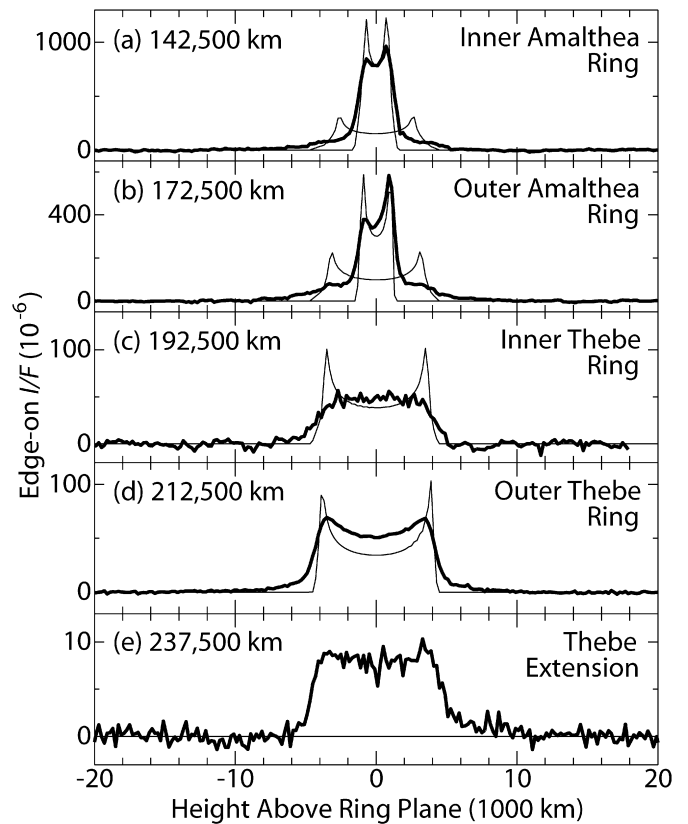


Fig. 13. A sequence of vertical profiles across the rings (heavy line), obtained from the C10 mosaic, is compared to the models for the Amalthea and Thebe rings (thin lines). Each profile is averaged over a 5000-km wide region. (a) The inner Amalthea ring at 140,000–145,000 km. (b) The outer Amalthea ring at 170,000–175,000 km. (c) The inner Thebe ring at 190,000–195,000 km. (d) The outer Thebe ring at 210,000–215,000 km. (e) The Thebe ring extension at 235,000–240,000 km. The peak locations in the Amalthea ring maintain a close alignment with the model's prediction, although faint portions of this ring extend vertically outward by  $\sim 1000$  km further [panels (a) and (b)]. The Thebe ring shows a much poorer fit to the predicted vertical profile. The peaks spread (d) and cease to exist as local maxima (c); in panel (b), the faintest material can be detected at least 6000 km from the ring plane, which is well above the predicted value.

The Amalthea ring's north–south asymmetry can be characterized further using other Galileo images. The C3 images (Fig. 1) appear symmetric, even though the C10 mosaic shows an asymmetry in this same region. The series of Europa images (Fig. 3), taken only 2.5 h before the C10 mosaic, does show an asymmetry. These images view the opposite ansa and show the southern half of the ring to be  $\sim 25\%$  brighter. This suggests that the material is concentrated in an inclined plane, which is tilted northward on the east ansa and southward on the west. This will be discussed further below.

Fig. 14 provides another view of the rings' vertical structure. Fig. 14a shows the north and south peak locations in the Amalthea ring's vertical profile, as a function of projected distance from the planet. Measurements are compared to the peak locations in the corresponding pseudo-image. The figure shows a very close alignment between measurement and prediction, including a correlation between thickness and radius that indicates inclinations are conserved. We believe that the small but

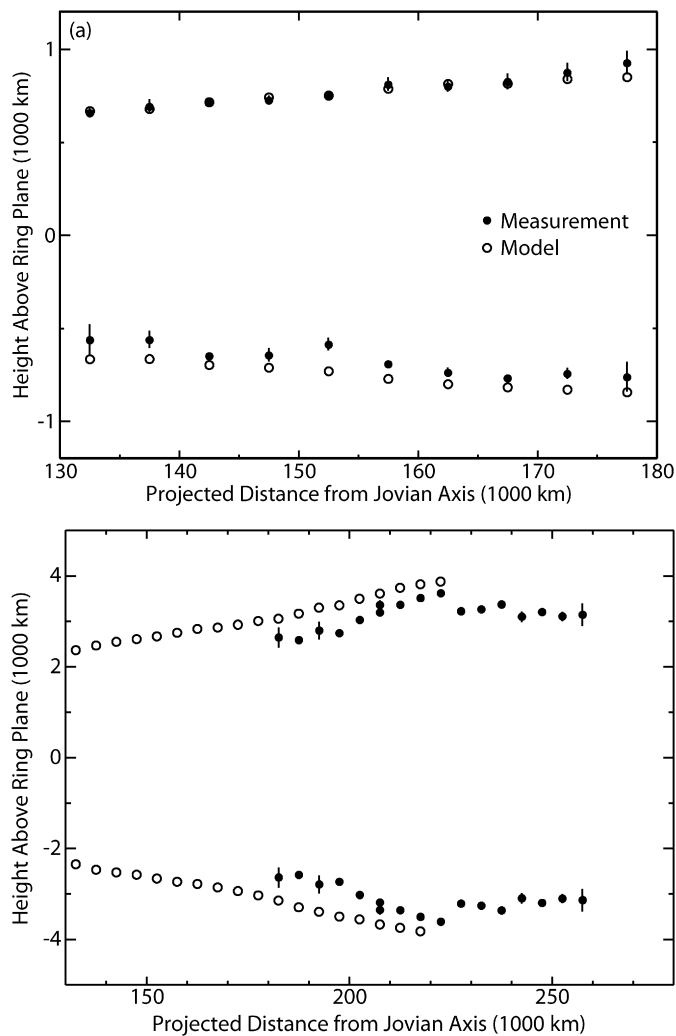


Fig. 14. The vertical peaks of each ring (solid circles) are compared to the models (open circles). Error bars of  $\pm$  one standard deviation have been plotted for each measurement, although many of these bars are smaller than the points. The Amalthea ring (a) shows a very close alignment between measurements and predictions. The systematic offset of the southern points is probably caused by the Thebe ring's underlying contribution, which distorts the vertical profiles but affects the southern peaks more than the sharper northern peaks. Because the Thebe ring (b) is so weakly peaked, these measurements indicate the location where the slope of the vertical profile changes most rapidly. The north and south Thebe ring measurements have been averaged to improve precision. Although all measurements are systematically closer to the equator than the model's predictions, the ring does show the characteristic linear change of thickness with radius, indicating that mean inclination is conserved. The Thebe extension beyond 225,000 km shows a roughly constant thickness instead.

systematic offset in the southern peak location is not significant; it arises from the fact that the measured southern peaks are not as sharp as in the model, so they tend to be displaced toward the equator by the underlying variations. Because the northern peaks are sharper and taller, they are less altered by this effect.

Fig. 14b shows estimated peak locations for Thebe's ring. This ring's profile does not show sharp peaks (Fig. 13), so the measurements instead locate the position where the profile bends most sharply. Although these measurements are systematically offset inward relative to the model, the variation of

thickness with radius is again observed. This confirms that the grains in Thebe's ring also tend to conserve their inclinations. Somewhat unexpectedly, the Thebe ring's outer extension outward beyond 225,000 km does not show any correlation of thickness with radius, contradicting the trend that one would predict if inclination is conserved.

The key conclusion to be drawn here is that several different processes must be at work. Some grains are scattered vertically while others are not. The most likely discriminator is particle size—perhaps the largest grains evolve inward exclusively under PR drag, while smaller grains are scattered vertically under the influence of electromagnetic perturbations. The additional material detected at heights beyond the nominal thickness probably comprises the smallest grains, which are most sensitive to electromagnetic perturbations.

#### 4.4. Cross-sectional views

The figures shown so far are comparisons between the model and the data, showing some agreements and some disagreements. The form of the rings would be easier to interpret if we could derive the 3-D structure directly, taking advantage of the low optical depth and expected axial symmetry. This is possible via the inverse Abel Transform, or by a numerical technique we refer to more colloquially as “onion peeling” (cf. de Pater et al., 1999). The concept is that we can divide the ring up into cylindrical shells and, starting from the outermost shell, derive its local density and subtract that shell's contribution from each interior shell. The process converts an edge-on image to a cross-sectional slice through the ring. The problem with this method is that it is akin to differentiation and so increases the noise in the data considerably. As a result, it can only be applied when SNR is high. Lower-SNR data can sometimes be onion-peeled successfully by first smoothing the data and/or converting it from an image to a vertically-integrated radial profile. Note that the procedure can only be used when the outer tip of the ring is visible, so the C3 ring and Europa images cannot be processed in this manner.

The most detailed and sensitive ring detection of the gossamer rings is from the C10 mosaic. The one complication here is that the scattering angle  $\theta \equiv 180^\circ - \alpha$  decreases from left to right across the mosaic;  $\theta = 2.4^\circ$  near the Thebe ring's outer tip but  $1.2^\circ$  where the Amalthea ring meets the main ring. This is because the Sun was behind Jupiter when the images were taken, so features at larger distances from Jupiter also have larger angular offsets from the Sun, and hence larger values of  $\theta$ . For a typical population of fine dust, the ring would be expected to brighten by a factor of 3–30 within this range; our photometry predicts a factor of 10 but it is unclear whether the phase function should be the same throughout the Thebe and Amalthea rings. To allow for this uncertainty we have generated cross-sectional profiles for a range of different assumptions about the phase factor across the image. Although the absolute brightness of each image varies as a result of the different assumptions, the overall appearances are quite similar. Fig. 15 shows the result when the assumed factor is 10. Because of the uncertainty, however,

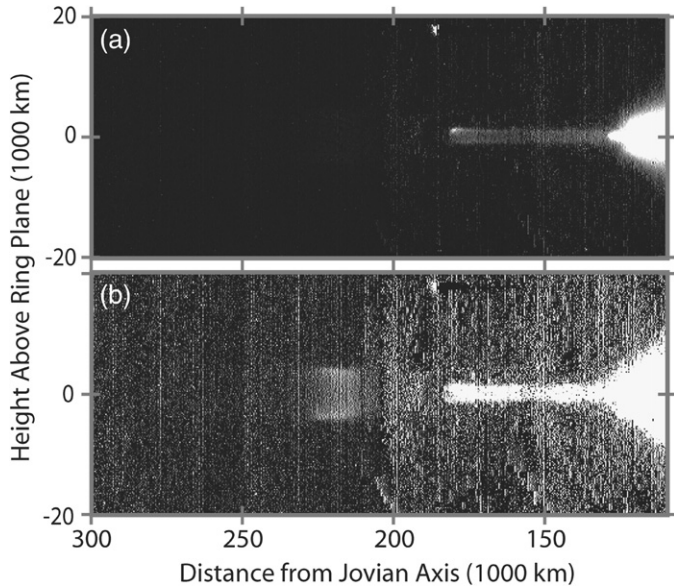


Fig. 15. An “onion-peeled” version of the C10 mosaic. The same image is shown with two enhancements, one emphasizing the Amalthea ring (a) and the other emphasizing the Thebe ring (b). The most surprising feature of Amalthea’s ring is a bright concentration near the northern tip, which is visible as an asymmetry in Fig. 2. The Thebe ring may show an inner edge, but this is uncertain because it falls so close to the border between two images of the mosaic.

this image is suitable for geometric analysis and for qualitative photometry, but not for absolute measurements of intensity.

Most notable in Fig. 15 is the bright feature at the northern tip of Amalthea’s ring. This is apparent in the unprocessed image (Figs. 3 and 11) but here we learn that it is highly localized near the orbit of Amalthea itself. Fig. 16a provides a more quantitative comparison. The peak is shifted inward by  $\sim 1000$  km and it damps out rapidly from there, vanishing within 5000 km. Its inward extension might be an artifact, however, because noise and other imperfections in the onion-peeling process sometimes produce these extensions interior to localized, bright features. Aside from this asymmetric peak, the overall profile of the Amalthea ring is quite uniform, supporting the model of dust evolving inward at a fixed rate under PR drag.

Because the onion-peeled image is much noisier than the original, the Thebe ring’s outward extension has disappeared. The Thebe ring itself is lost at the border between images comprising the mosaic. Nevertheless, a radial profile of the ring (Fig. 16b) shows a strong peak at or just interior to the orbit of Thebe, much like the one near Amalthea’s orbit. The peaks are qualitatively quite similar, suggesting that a common physical process might be at work. However, the peaks have one fundamental difference—Amalthea’s peak is entirely displaced northward from the equator, whereas Thebe’s peak appears to be more symmetric about the ring plane. This puzzling discrepancy will be discussed further below.

An onion-peeled version of the ACS profile for the Amalthea ring is shown in Fig. 17. The profile has been low-pass filtered

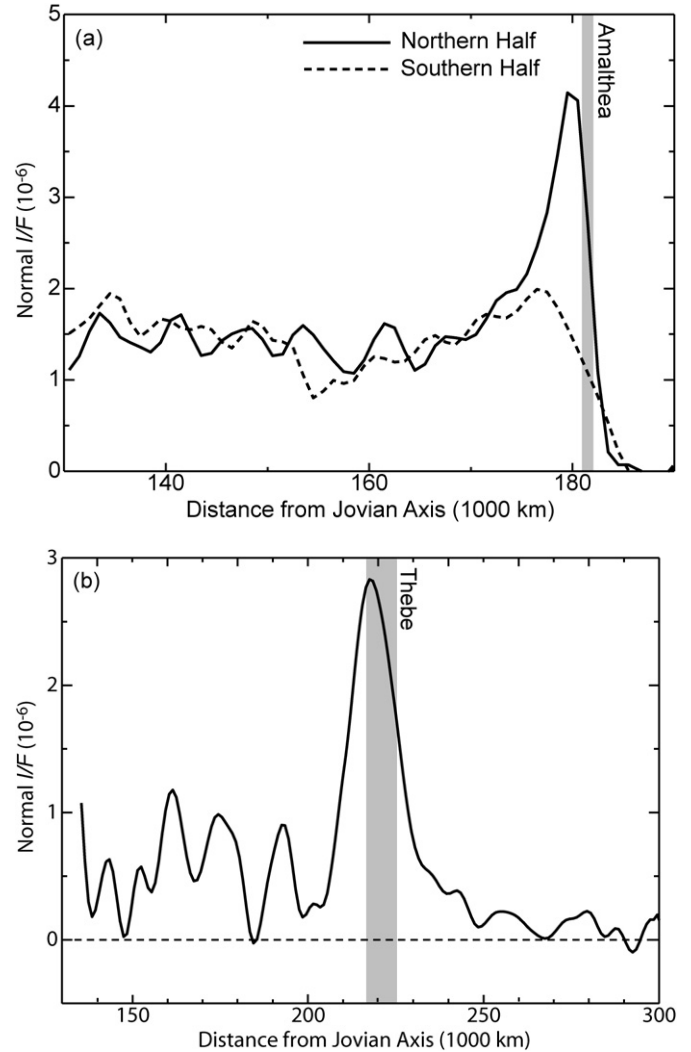


Fig. 16. Smoothed and then onion-peeled versions of the rings’ vertically integrated radial profiles from Galileo’s C10 mosaic (cf. Fig. 11). (a) The Amalthea ring is again shown as northern and southern halves. We see clearly that the strong peak is located close but interior to the orbit of Amalthea, and that the remainder of the ring shows the uniform radial profile consistent with our model. (b) The Thebe ring’s profile shows a more convincing inner limit, where the ring’s density suddenly drops by perhaps a factor of three. In many ways, this profile is similar to that of the Amalthea ring, suggesting common processes at work. Due to the extensive processing that has gone into these profiles, the uncertainty in any point is highly correlated with that of its neighbors. For this reason, reliable error bars are difficult to estimate, so none are plotted in the figure. However, the amplitude of the smooth variations inward from each peak can be construed as representative of the general uncertainties. The peaks are clearly several times larger than these variations, and therefore statistically significant.

prior to the inversion to reduce noise; however, this filtering contributes to the broad residual oscillations visible. Nevertheless, the resulting profile shows properties very similar to those found in the Galileo data and in earlier Keck data analysis (de Pater et al., 1999). Specifically, the peak of the ring does not coincide with Amalthea’s orbit; instead, it is displaced inward by  $\sim 2000$  km (Fig. 17). Unfortunately, the SNR in our profile of Thebe’s ring is too noisy for us to carry out a similar analysis.

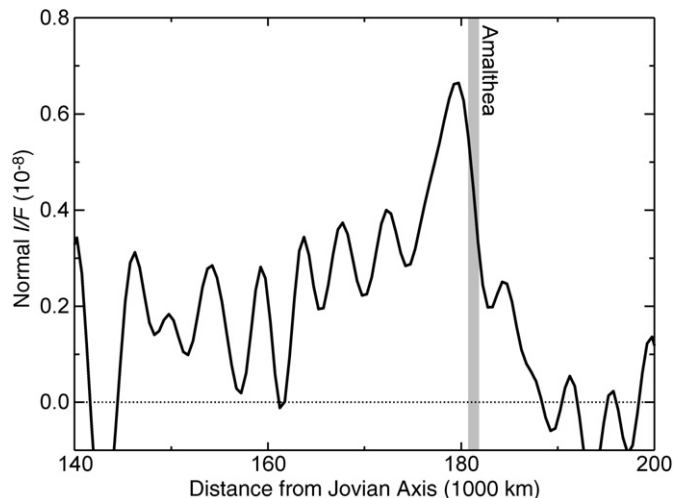


Fig. 17. An onion-peeled profile of Amalthea's ring, derived from the Hubble ACS images (cf. Fig. 12). The profile is very similar to that from Galileo (Fig. 16), with a marked peak just interior to Amalthea's orbit and a generally uniform (although noisy) trend inward from there. To reduce the noise, the edge-on profile was smoothed to 2000-km resolution prior to the onion-peel processing; the inner, quasi-periodic variations are an artifact of this smoothing. As in the case of Fig. 16, quantitative error bars are difficult to determine and are not plotted.

## 5. Discussion

### 5.1. Overview

In general terms, the images of the gossamer rings provide significant support for the model of dust evolving uniformly inward under PR drag. Both rings are fairly uniform in cross-section inward from their (unpredicted) outer peaks. Both show concentrations north and south of the equator plane, with vertical separations that decrease in proportion to radius; this indicates that the mean inclination of the inward-evolving grains is conserved. The power-law size distribution with  $q = 2-2.5$  is compatible with collisional ejecta evolving under a drag force (cf. Burns et al., 1984).

Nevertheless, the data provide some puzzling additional details about the rings. Most notable are the strong peaks just interior to each moon. This probably accounts for the sudden drop in dust impacts during Galileo's traversal through the Thebe ring (Krüger, 2003; Krüger et al., 2003, 2005). The north-south asymmetry of Amalthea's peak, needs to be explained; Thebe's ring does not share this property. Some grains are scattered vertically relative to their initial inclinations, although most deviations are small. The outward extension to Thebe's ring was not expected, and we now learn that Amalthea's ring has no analogous feature of comparable magnitude.

### 5.2. Peaks and vertical asymmetry

The apparent north-south asymmetry of the Amalthea ring requires an explanation. One might suppose that this is a geometric effect—from Galileo's viewpoint, the effective ring opening angle  $B$  will be slightly different for the northern and southern limits of the ring. However, first note that this dif-

ference is very small,  $0.0004^\circ$  relative to a mean  $B$  of  $0.153^\circ$  (Table 1). Second, recall that the area under the intensity curve  $I(z)$  should be independent of  $B$  when  $B$  is small; changes in  $B$  will alter the width and height of each peak, but the area under the curve is conserved. In these rings, the optical depth is so low that every particle is always visible, regardless of  $B$ . As Fig. 11a and panel (b) of Fig. 13 illustrate, the areas under the northern and southern halves of the Amalthea ring are distinctly different. We must therefore seek an alternative explanation.

Fig. 18 shows the orbits of Amalthea and Thebe as seen from Galileo at the time of the C10 mosaic. The figure has been constructed by time-shifting each moon in its orbit by multiples of 1000 s, while Galileo's viewpoint remains fixed. At the time of this mosaic, three properties of the viewing geometry on Amalthea's orbit were distinctive. First, Amalthea's orbit was nearly edge-on to Galileo, so that any concentration of material in its orbit would have been especially bright. Second, Galileo was positioned near the orbit's node, so that the tip of the orbit is displaced to its northernmost extreme in the image. And third, at the time of the image Amalthea fell  $6000$  s, or  $\sim 50^\circ$ , behind the ansa. All of these factors point to a simple explanation for the bright feature observed: a concentration of material trapped in Amalthea's leading Lagrange point!

The enhancement seen at the southern tip in the Europa images (Fig. 3) of the opposite ansa further supports the concentration in an inclined plane. These images were taken 2.5 h earlier than the C10 mosaic. Galileo's viewpoint changed rather little in this time, but Amalthea advanced by  $\sim 80^\circ$ . As a result, Amalthea was  $\sim 50^\circ$  ahead of the ansa in these images, suggesting a similar concentration at the trailing Lagrange point. The amplitude of the asymmetry is smaller in these images, but that is probably due to the fact that we do not see the ring tip, where the asymmetry would be largest. Because we do not see the ring at other longitudes, we cannot determine whether the ring dust "horseshoes" back and forth between the two Lagrange points.

For comparison, Fig. 18b shows that Thebe's orbit was far from edge-on to Galileo. Furthermore, it was 19,000 s or  $117^\circ$  from the ansa at the time. Thus, any analogous concentration in Thebe's orbit, if it exists, would not have been detected in this image. Because of the lower SNR and coarser resolution of the Earth-based data sets, it is unlikely that they could detect significant asymmetries.

A plausible conclusion is that each gossamer ring actually consists of two populations. One is ejecta trapped in the orbit of its source moon via a 1:1 resonance. This material would retain the inclination and node of the moon's orbit and would tend to be concentrated near the Lagrange points, which can be longitudinally extended but are centered on points leading and trailing the moon by  $\sim 60^\circ$ . Note that a similar explanation was once proposed for Jupiter's main ring and for the narrow uranian rings (Dermott et al., 1980; Dermott and Murray, 1980). The second population is material that has escaped from resonance and is evolving inward, with PR drag being the dominant driving force.

However, the role of the 1:1 resonance appears to be contradicted by the fact that the ring peaks are displaced inward from the orbits of Amalthea and Thebe. In the edge-on images,

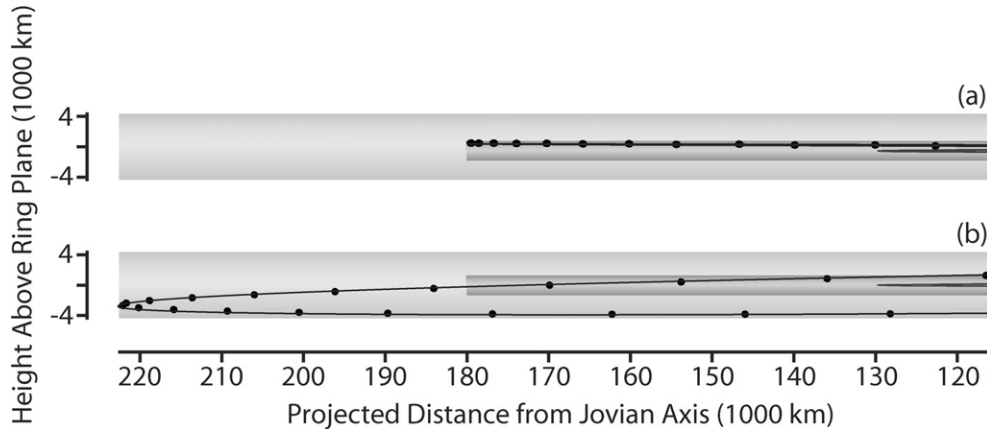


Fig. 18. The orbits of Amalthea and Thebe as seen from vantage point of Galileo during the C10 mosaic. The position of each moon is plotted at 1000-s intervals while holding Galileo at its fixed location. The figure illustrates that Galileo was located near the descending node of Amalthea's orbit (a), where the orbit is seen nearly edge-on. However, Galileo's position has no particular significance relative to the node of Thebe's orbit (b). Gray bands represent the Amalthea and Thebe rings, and the central band at right is the main ring.

this would be expected as a simple projection effect. However, one would expect the onion-peeled versions of the profiles to show a closer alignment of the peak with the moon's orbit. For Amalthea, the explanation may be related to the fact that the onion-peeling process assumes a circularly symmetric ring, whereas in reality material is concentrated around the Lagrange points. Because Amalthea was  $50^\circ$  from the ansa at the time of the C10 mosaic, its Lagrange point was  $10^\circ$  off the ansa. Thus, any material at the Lagrange point would appear to be displaced inward from the ring tip by a distance  $r_0[1 - \cos(10^\circ)]$ . This distance is  $\sim 2800$  km, which is quite consistent with the offset in Fig. 16a.

The offset in the peak of the Thebe ring requires a different explanation, however, because the moon and its Lagrange points do not fall near the ansa. However, Thebe has a large eccentricity and a check of the ephemeris reveals that its orbit was oriented with its pericenter near the ansa in the C10 mosaic. Thebe's radial distance at the ansa was 218,600 km, not its mean value of 221,900 km. As a result, the peak of the ring does, in fact, fall atop Thebe's orbit at the time of the C10 observations!

The data are therefore all consistent with concentrations of ring material locked in 1:1 resonances with both Amalthea and Thebe. Such a resonance locks both the pericenter and the node of the ring material with that of the source moon, so it predicts the vertical asymmetry at the tip of Amalthea's ring and the inward shift of the peak in Thebe's ring. If Amalthea's material is concentrated near its Lagrange points, then the apparent radial shift of its peak is also explained.

However, it is also worthwhile to consider briefly an alternative hypothesis, which is that the bright clump represents a transient phenomenon, perhaps due to a relatively recent, large impact into Amalthea. The fact that the particles are all displaced northward means that the nodes of these orbits have not yet had time to randomize, and this places a rather strict upper limit on how recently the impact could have occurred. We can estimate that the velocity of ejecta from Amalthea is compar-

able to Amalthea's escape velocity, 88 m/s (Burns et al., 1999). Amalthea's orbital velocity is 26.4 km/s, so the ejecta undergoes a fractional change in velocity of 0.33% and a fractional change in semimajor axis of 0.66%. It can be shown that this changes the nodal regression rate by  $0.057^\circ/\text{day}$ , so the nodes of ejecta will be fully distributed in longitude within  $180/0.057$  days or  $\sim 9$  years. Fig. 16a shows that the additional dust essentially doubled the brightness of the ring's outer tip. It is difficult to estimate the size or flux of impactors necessary to generate this much additional dust, but if this was a typical impact, then one should expect substantial variations in the brightness of the gossamer rings over decadal time scales. While this idea has much less predictive power than the 1:1 resonance model, both hypotheses can be tested with future observations.

### 5.3. Orbital evolution

Dust that escapes from, or perhaps never enters, each moon's 1:1 resonance begins its journey inward under PR drag. In general, the particles observed in the gossamer rings are quite large compared to those in other dusty rings. This is primarily a selection effect due to the high phase angles observed by Galileo and Voyager, which emphasize particles 4–30  $\mu\text{m}$  in size. This has significant implications for the rings' dynamics.

Dust grains as large as 10–30  $\mu\text{m}$  are essentially immune to Lorentz forces. They respond to PR drag, but on time scales of a few  $\times 10^6$  years (Burns et al., 2001, see their Table 2). The other pertinent times are collisional fragmentation ( $10^{3\pm 1}$  years) and sputtering ( $10^{5\pm 1}$  years). Neither of these is well constrained but both imply problems for such large grains, because they are destroyed faster than they travel inward. Perhaps these are part of the particle populations just interior to the two moons. If so, then the radial widths provide a rough indication of the relative speeds of evolution versus removal.

Smaller grains are less emphasized by the high phase angles of the Galileo data, but they are not invisible. These evolve more rapidly under PR drag and are less subject to fragmentation, so

they are more plausible constituents of the more uniform regions of each ring. However, such grains *do* respond to Lorentz forces. The region interior to Amalthea's orbit is free of strong Lorentz resonances, which is consistent with the fact that the particles in this ring appear to maintain their inclinations as they evolve inward.

The Thebe ring is very different in this regard. Thebe grains must cross the 2:3, 3:4, and 4:5 resonances (at 209,900, 194,000, and 185,900 km, respectively). The strong vertical perturbations at these locations probably account for the greater and more random vertical distribution of Thebe's ring. Very small grains may get trapped by these resonances and/or scattered out of the system. However, most such grains are probably smaller than our detection threshold at the C10 viewing geometry. See Hamilton (2003) and especially Section 11.4.2 of Burns et al. (2004) for a more extensive discussion of these resonances and their effects.

Hamilton (2003) has recently proposed a plausible explanation for the Thebe ring's outward extension. He invokes a shadow resonance, first investigated by Horanyi and Burns (1991). In brief, photoelectric processes shut down when a grain passes through the planet's shadow, so a grain's electric charge varies in synchrony with its orbital motion. Lorentz forces drive periodic oscillations in the orbital eccentricity and semimajor axis of these grains, which results in large radial excursions from the source moon. This explains how material can reach radial distances far beyond the orbit of Thebe. However, there is no corresponding oscillation of the inclinations, so the dispersed grains retain the vertical thickness of the ring. This simple scenario seems to provide a perfect match to the Thebe ring's observed extension. Re-collisions with the source moon might make this entire system self-sustaining, reducing the dependence on incoming micrometeoroids to inject new material into the ring (cf. Hamilton and Burns, 1994).

The shadow resonance that nicely predicts the outward extension of the Thebe ring (Hamilton, 2003) also implies that Amalthea material should spread outward from its source satellite, but this is not seen in the data. Two factors account for this. First, grains in both ring extensions must continue to cross the orbit of their source moons; the time scale for re-collision is  $\sim 3000$  years for Thebe's material but only 100 years for Amalthea's. All else being equal, this predicts a 30-fold reduction in the relative brightness of Amalthea's extension. Second, the shadow resonance is much weaker at Amalthea than at Thebe, because the satellite is located only 10% beyond synchronous orbit, where electromagnetic forces disappear. This means that a broader range of dust grains sizes should populate the Amalthea extension. Simulations show that the inclination histories of different-sized Amalthea grains vary widely; the 1.5  $\mu\text{m}$  grains that can reach Thebe's orbit attain inclinations of up to a degree. Thus the outward extension from Amalthea would not bear Amalthea's distinctive inclination signature. In summary, any outward extension to the Amalthea ring is both much fainter and much broader than the Thebe ring's extension, rendering it undetectable atop the Thebe ring.

#### 5.4. Conclusions

We have combined all of the available image data to derive a surprising amount of information about the jovian gossamer rings, including their particle sizes and details of their 3-D structure. In general, the model of Burns et al. (1999), see also Ockert-Bell et al. (1999), is supported—most of the ring's structure can be accounted for by dust ejected from the source moons, Amalthea and Thebe, which then evolve inward under Poynting–Robertson drag.

The most significant discrepancy between this model and the rings' detailed structure is that each ring contains a large concentration of dust near or just interior to its own orbit. The observations are all consistent with material trapped in a 1:1 resonance with each source moon. Amalthea's trapped material appears to have remained node-locked to Amalthea's orbital plane, and Thebe's material retains the orbital pericenter of its source body.

We argue that most of the remaining discrepancies between the theory and the observations can be accounted for by the effects of Lorentz perturbations on the ring grains. The Thebe ring's tiniest grains disperse vertically during their journey inward, probably due to vertical perturbations from several strong Lorentz resonances. The outward extension to the Thebe ring is probably caused by small grains in Thebe's ring that receive large eccentricities due to a shadow resonance.

#### Acknowledgments

Support for Hubble Space Telescope program number GO-9426 was provided by NASA through a grant from the Space Telescope Science Institute, which is operated by the Association of Universities for Research in Astronomy, Incorporated, under NASA contract NAS5-26555. NASA's Planetary Geology and Geophysics Program supported this work through grant NNG05GL48G to the SETI Institute, RTOP 344-30-21-04 to NASA Ames, and Grant NAGW-310 to Cornell University. NASA also supported this work through Planetary Astronomy grant NAG 5-13370 to the University of California, Berkeley and Exobiology grant NNG04GM18G to the University of Maryland. We are grateful to Henry Throop for a comprehensive and constructive review of this paper. Our friend and colleague Damon Simonelli played a major role in the design and implementation of the Galileo imaging of Jupiter's rings and inner moons. We like to think he would have enjoyed learning about the debris clouds generated by two of his favorite "potatoes." We dedicate this article to his memory.

#### References

- American Society for Testing and Materials, 2000. ASTM Standard Extraterrestrial Spectrum Reference E-490-00.
- Anderson, J., King, I.R., 2004. Multi-filter PSFs and distortion corrections for the HRC. Instrument Science Report ACS 2004-15, Space Telescope Science Institute.
- Brooks, S.M., Esposito, L.W., Showalter, M.R., Throop, H.B., 2004. The size distribution in Jupiter's main ring from Galileo imaging and spectroscopy. *Icarus* 170, 35–57.

- Brown, R.H., Baines, K.H., Bellucci, G., Bibring, J.-P., Buratti, B.J., Capaccioni, F., Cerroni, P., Clark, R.N., Coradini, A., Cruikshank, D.P., Drossart, P., Formisano, V., Jaumann, R., Langevin, Y., Matson, D.L., McCord, T.B., Mennella, V., Nelson, R.M., Nicholson, P.D., Sicardy, B., Sotin, C., Chamberlain, M.C., Hansen, G., Hibbitts, K., Showalter, M., 2003. Observations with the Visual and Infrared Mapping Spectrometer (VIMS) during Cassini's flyby of Jupiter. *Icarus* 164, 461–470.
- Burns, J.A., Showalter, M.R., Morfill, G., 1984. The ethereal rings of Jupiter and Saturn. In: Greenberg, R., Brahic, A. (Eds.), *Planetary Rings*. University of Arizona Press, Tucson, pp. 200–272.
- Burns, J.A., Showalter, M.R., Hamilton, D.P., Nicholson, P.D., de Pater, I., Ockert-Bell, M., Thomas, P., 1999. The formation of Jupiter's faint rings. *Science* 284, 1146–1150.
- Burns, J.A., Hamilton, D.P., Showalter, M.R., 2001. Dusty rings and circumplanetary dust: Observations and simple physics. In: Grün, E., Gustafson, B.A.S., Dermott, S.F., Fechtig, H. (Eds.), *Interplanetary Dust*. Springer-Verlag, Berlin, pp. 641–725.
- Burns, J.A., Simonelli, D.P., Showalter, M.R., Hamilton, D.P., Porco, C.C., Throop, H., Esposito, L.W., 2004. Jupiter's ring-moon system. In: Bagenal, F. (Ed.), *Jupiter: The Planet, Satellites and Magnetosphere*. Cambridge University Press, Cambridge, pp. 241–262.
- Colina, L., Bohlin, R.C., Castelli, F., 1996. The 0.12–0.25 micron absolute flux distribution of the Sun for comparison with solar analog stars. *Astron. J.* 112, 307–315.
- de Pater, I., Showalter, M.R., Burns, J.A., Nicholson, P.D., Liu, M.C., Hamilton, D.P., Graham, J.R., 1999. Keck infrared observations of Jupiter's ring system near Earth's 1997 ring plane crossing. *Icarus* 138, 214–223.
- de Pater, I., Showalter, M.R., Macintosh, B., 2008. Structure of the jovian ring from RPX 2002–2003 Keck data. *Icarus*, in press (this issue).
- Dermott, S.F., Murray, C.D., 1980. Origin of the eccentricity gradient and apse alignment of the  $\epsilon$  ring of Uranus. *Icarus* 43, 338–349.
- Dermott, S.F., Murray, C.D., Sinclair, A.T., 1980. The narrow rings of Jupiter, Saturn and Uranus. *Nature* 284, 309–313.
- Dohnanyi, J.S., 1972. Interplanetary objects in review: Statistics of their masses and dynamics. *Icarus* 17, 1–48.
- Gradie, J., Thomas, P., Veverka, J., 1980. The surface composition of Amalthea. *Icarus* 44, 373–387.
- Graham, J.R., Matthews, K., Soifer, B.T., Nelson, J.E., Harrison, W., Jernigan, J.G., Lin, S., Neugebauer, G., Smith, G., Ziomkowski, C., 1994. Infrared observations of the  $Z = 3.8$  radio galaxy, 4C 41.17, with the W.M. Keck telescope. *Astrophys. J.* 420, L5–L8.
- Hamilton, D.P., 2003. Jupiter's gossamer rings explained. *Bull. Am. Astron. Soc.* 35, 930.
- Hamilton, D.P., Burns, J.A., 1994. Origin of Saturn's E ring: Self-sustained, naturally. *Science* 264, 550–553.
- Hamilton, D.P., Burns, J.A., Nicholson, P.D., Showalter, M.R., de Pater, I., 1998. Do Jupiter's gossamer rings have vertically-extended halos? *Bull. Am. Astron. Soc.* 30, 1040.
- Horanyi, M., Burns, J.A., 1991. Charged dust dynamics: Orbital resonance due to planetary shadows. *J. Geophys. Res.* 96, 19283–19289.
- Horanyi, M., Burns, J.A., Hamilton, D.P., 1992. The dynamics of Saturn's E ring particles. *Icarus* 97, 248–259.
- Krüger, H., 2003. *Jupiter's Dust Disc: An Astrophysical Laboratory*. Shaker-Verlag, Aachen, ISBN 3-8322-2224-3.
- Krüger, H., Grün, E., Hamilton, D.P., 2003. Galileo in-situ dust measurements in Jupiter's gossamer rings. *Bull. Am. Astron. Soc.* 35, 20.05.
- Krüger, H., Grün, E., Hamilton, D.P., 2005. Galileo in-situ dust measurements in Jupiter's gossamer rings. In: *Proceedings of the Workshop Dust in Planetary Systems*, Kauai, Hawaii, September 26–28, 2005, p. 101.
- Matthews, K., Soifer, B.T., 1994. The near-infrared camera on the W.M. Keck telescope. In: McLean, I.S. (Ed.), *Infrared Arrays in Astronomy: The Next Generation*. Kluwer, Dordrecht, pp. 239–246.
- McMudroch, S., Pilorz, S.H., Danielson, G.E., and the NIMS Science Team, 2000. Galileo NIMS near-infrared observations of Jupiter's ring system. *Icarus* 146, 1–11.
- Nicholson, P.D., Showalter, M.R., Dones, L., French, R.G., Larson, S.M., Lissauer, J.J., McGhee, C.A., Seitzer, P., Sicardy, B., Danielson, G.E., 1996. Observations of Saturn's ring plane crossings in August and November 1995. *Science* 272, 509–515.
- Ockert-Bell, M., Burns, J.A., Daubar, I.J., Thomas, P.C., Belton, M.J.S., Klaasen, K.P., 1999. The structure of Jupiter's ring system as revealed by the Galileo imaging experiment. *Icarus* 138, 188–213.
- Pavlovsky, C., Biretta, J., Boffi, F., Bohlin, R., Cox, C., Fruchter, A., Giavalisco, M., Gilliland, R., Gonzaga, S., Heyer, I., Hook, R., Joglee, S., Koekemoer, A., Mack, J., Mutchler, M., Platais, V., Riess, A., Sirianni, M., van der Marel, R., van Orsow, D., 2005. *ACS Data Handbook*. STScI, Baltimore.
- Persson, S.E., Murphy, D.C., Krzeminski, W., Roth, M., Rieke, M.J., 1998. A new system of faint near-infrared standard stars. *Astron. J.* 116, 2475–2488.
- Pollack, J.B., Cuzzi, J.N., 1980. Scattering by nonspherical particles of size comparable to a wavelength: A new semi-empirical theory and its application to tropospheric aerosols. *J. Atmos. Sci.* 37, 868–881.
- Pollack, J.B., Hollenbach, D., Becwith, S., Simonelli, D.P., Roush, T., Fong, W., 1994. Composition and radiative properties of grains in molecular clouds and accretion disks. *Astrophys. J.* 421, 615–639.
- Porco, C.C., West, R.A., McEwen, A., Del Genio, A.D., Ingersoll, A.P., Thomas, P., Squyres, S., Dones, L., Murray, C.D., Johnson, T.V., Burns, J.A., Brahic, A., Neukum, G., Joseph Veverka, Barbara, J.M., Denk, T., Evans, M., Ferrier, J.J., Geissler, P., Helfenstein, P., Roatsch, T., Throop, H., Tiscareno, M., Vasavada, A.R., 2003. Cassini imaging of Jupiter's atmosphere, satellites, and rings. *Science* 299, 1541–1547.
- Showalter, M.R., Burns, J.A., Cuzzi, J.N., Pollack, J.B., 1985. The discovery of Jupiter's 'gossamer' ring. *Nature* 316, 526–528.
- Showalter, M.R., Burns, J.A., Cuzzi, J.N., Pollack, J.B., 1987. Jupiter's ring system: New results on structure and particle properties. *Icarus* 69, 458–498.
- Showalter, M.R., Cuzzi, J.N., Larson, S.M., 1991. Structure and particle properties of Saturn's E ring. *Icarus* 94, 451–473.
- Showalter, M.R., Pollack, J.B., Ockert, M.E., Doyle, L., Dalton, J.B., 1992. A photometric study of Saturn's F ring. *Icarus* 100, 394–411.
- Showalter, M.R., Burns, J.A., de Pater, I., Hamilton, D.P., Horanyi, M., 2003. Recent Hubble observations of Jupiter's ring system. *Bull. Am. Astron. Soc.* 35, 930.
- Showalter, M.R., Burns, J.A., de Pater, I., Hamilton, D.P., Horanyi, M., 2005. Jupiter's ring system: New results from Galileo, Voyager, Hubble and the Keck Telescope. In: *Presentation at the ISSI Workshop on the Physics of Dusty Rings*, Bern, Switzerland, June 20–24.
- Thomas, P.C., Burns, J.A., Rossier, L., Simonelli, D., Veverka, J., Chapman, C.R., Klaasen, K., Johnson, T.V., Belton, M.J.S., and the Galileo Imaging Team, 1998. The small inner satellites of Jupiter. *Icarus* 135, 360–371.
- Throop, H.B., Porco, C.C., West, R.A., Burns, J.A., Showalter, M.R., Nicholson, P.D., 2004. The jovian rings: New results derived from Cassini, Galileo, Voyager and Earth-based observations. *Icarus* 172, 59–77.
- Wong, M.H., de Pater, I., Showalter, M.R., Roe, H.G., Macintosh, B., Verbanac, G., 2006. Ground-based near infrared spectroscopy of Jupiter's ring and moons. *Icarus* 185, 403–415.